Electron transfer between anatase TiO_2 and an O_2 molecule directly observed by atomic force microscopy

Martin Setvin[a,1], Jan Hulva[a], Gareth S. Parkinson[a], Michael Schmid[a], and Ulrike Diebold[a]

[a]Institute of Applied Physics, TU Wien, 1040 Vienna, Austria

Edited by Thomas E. Mallouk, The Pennsylvania State University, University Park, PA, and approved February 14, 2017 (received for review November 11, 2016)

Activation of molecular oxygen is a key step in converting fuels into energy, but there is precious little experimental insight into how the process proceeds at the atomic scale. Here, we show that a combined atomic force microscopy/scanning tunneling microscopy (AFM/STM) experiment can both distinguish neutral O_2 molecules in the triplet state from negatively charged $(O_2)^-$ radicals and charge and discharge the molecules at will. By measuring the chemical forces above the different species adsorbed on an anatase TiO_2 surface, we show that the tip-generated $(O_2)^-$ radicals are identical to those created when (*i*) an O_2 molecule accepts an electron from a near-surface dopant or (*ii*) when a photo-generated electron is transferred following irradiation of the anatase sample with UV light. Kelvin probe spectroscopy measurements indicate that electron transfer between the TiO_2 and the adsorbed molecules is governed by competition between electron affinity of the physisorbed (triplet) O_2 and band bending induced by the $(O_2)^-$ radicals. Temperature–programmed desorption and X-ray photoelectron spectroscopy data provide information about thermal stability of the species, and confirm the chemical identification inferred from AFM/STM.

TiO_2 | anatase | AFM | O_2 | adsorption

Neutral O_2 molecules have a triplet spin configuration (1) and cannot form chemical bonds or enter chemical reactions with species in a singlet state (the vast majority of compounds). To become reactive, O_2 molecules need to be excited to the singlet state. Because this state lies 0.98 eV higher in energy (2), excitation is inefficient at room temperature but occurs, e.g., in combustion. Alternatively, O_2 can accept an electron. This process is not temperature-limited and is used by living organisms (via enzymes) (3, 4) and in technologies such as fuel cells and catalysis. Electron transfer into normally inert molecules (such as O_2, CO_2, or CH_4) is a key step toward their activation (5), yet direct experimental insights into this process are scarce, and appropriate theoretical tools are just under development (6, 7).

In recent years, combined atomic force microscopy/scanning tunneling microscopy (AFM/STM) has emerged as a powerful technique for investigating and manipulating the charge state of atoms and molecules. Gross et al. (8) have shown that the charge state of single Au atoms can be determined from Kelvin spectroscopy, and that electrons can be deliberately injected and removed using the AFM/STM tip. Similar tip-induced charging/discharging processes have subsequently been demonstrated for other adsorbates, including organic molecules (9). In this work, we applied this approach to an anatase TiO_2 (101) surface covered with small amounts of molecular O_2.

A mixture of neutral and charged O_2 molecules form upon adsorption. The charge of the latter originates from near-surface dopants, albeit the resulting $(O_2)^-$ is not necessarily directly located directly above these dopants. The charged and uncharged molecules are clearly distinguished by their characteristic fingerprints in Kelvin probe spectroscopy. We directly measure chemical forces; the charged $(O_2)^-$ readily forms a chemical bond with the AFM tip, whereas neutral O_2 interacts only weakly. The charging of $(O_2)^-$ can also be achieved by injection of electrons from the tip, or by exposing this model photocatalytic system (10) to UV light. The microscopy results are complemented by area-averaging spectroscopy data, which reveal that the neutral O_2 species is present in the triplet state and desorbs at 64 K. Activated $(O_2)^-$, however, is chemisorbed and stable above room temperature. The band bending induced by the adsorbed $(O_2)^-$ species is determined from core-level peak shifts in X-ray photoelectron spectroscopy (XPS). We discuss our results with respect to previous work on the prototypical rutile TiO_2 (110) surface (11–24).

Results

When an anatase (101) surface is exposed to molecular O_2 at low temperature two types of adsorbates appear. Representative AFM images in Fig. 1 show faint, gray together with pronounced, dark spots; these are marked by black and red arrows, respectively. We will show that the faint spots are neutral O_2 molecules, and the dark spots are molecules that have spontaneously accepted an electron from the substrate. Throughout this paper we refer to the latter species as $(O_2)^-$ because our measurements are more consistent with the singly-charged (superoxo) than doubly charged (peroxo) state (25, 26). We note, however, that the experimental methods used here do not allow a precise quantification of the charge localized at a molecule. The $(O_2)^-$ are dominant at low coverages (Fig. 1*A*), but their concentration saturates at 1 to 2% of a monolayer (ML). All further O_2 molecules adsorb in neutral form (Fig. 1*C*).

The strong AFM contrast between the two species arises from their chemical reactivity. The $(O_2)^-$ readily forms a chemical bond with the tip, whereas the neutral O_2 is inert. Short-range

Significance

Molecular oxygen is an inert species, unable to enter chemical reactions. Activation occurs through the acceptance of an extra electron; this catalytic step plays a major role in applications such as heterogeneous catalysis and fuel cells. It is also used by all living organisms. We show that the two different charge states of O_2 can be easily distinguished by atomic force microscopy (AFM). We directly injected or removed electrons into/from the O_2 molecule by the AFM tip, switching the O_2 reactivity. These results open new possibilities for studying catalytic and photocatalytic processes.

Author contributions: M. Setvin, G.S.P., M. Schmid, and U.D. designed research; M. Setvin and J.H. performed research; M. Setvin and J.H. analyzed data; and M. Setvin, G.S.P., M. Schmid, and U.D. wrote the paper.

The authors declare no conflict of interest.

This article is a PNAS Direct Submission.

[1]To whom correspondence should be addressed. Email: setvin@iap.tuwien.ac.at.

This article contains supporting information online at www.pnas.org/lookup/suppl/doi:10.1073/pnas.1618723114/-/DCSupplemental.

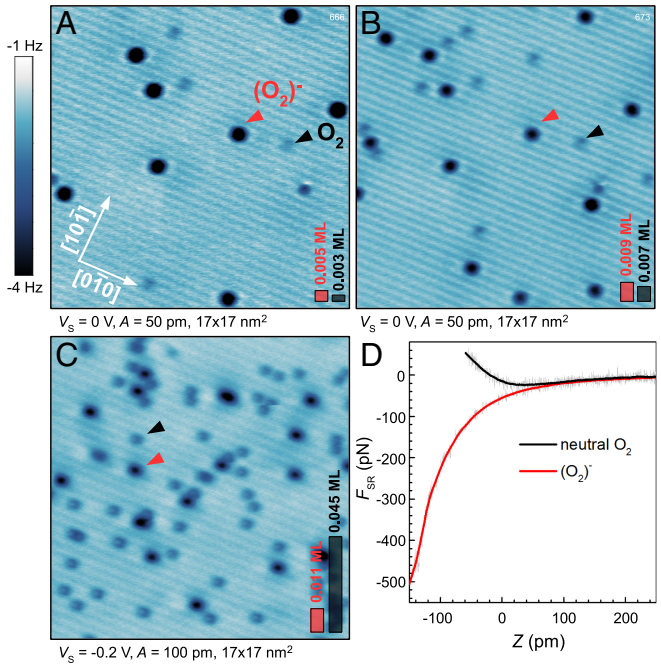

Fig. 1. Characterization of neutral and charged O_2 molecules by AFM. (*A*–*C*) Constant-height AFM images of O_2 adsorbed on the anatase (101) surface at T = 5.5 K. The total O_2 coverages are 0.008, 0.016, and 0.056 ML, respectively. Black arrows mark neutral O_2 molecules, and red arrows mark negatively charged $(O_2)^-$ species. Scale bars in the lower right corner reflect the concentration of the O_2 and $(O_2)^-$ in the imaged area. (*D*) Short-range chemical forces measured above the neutral and the charged O_2 molecules.

chemical forces measured above these species are plotted in Fig. 1*D*. The maximum attractive force above the neutral O_2 is of the order 20 pN, a weak interaction. The force measured above the $(O_2)^-$ is more than an order of magnitude higher and can be classified as a chemical bond with the tip. With most tips the minimum of the attractive force above the $(O_2)^-$ could not be reached because the molecule either dissociated or reacted with the tip.

All AFM images in this work are measured in the constant-height mode, where darker color reflects higher attractive force. This is necessary to avoid unintended interactions with the weakly adsorbed neutral O_2 species, for example pulling it across the surface or picking it up with the tip. The contrast in AFM images is tip-dependent, and throughout this paper we present images acquired with reactive tips, likely Ti-terminated (27). Other tip terminations are discussed in *Supporting Information* (Fig. S1), along with AFM images of the clean anatase substrate (Fig. S2). The Δf scale shown next to Fig. 1*A* is similar in all further AFM images in the main text. Precise scale bars are shown in *Supporting Information*.

When imaging the surface it is important to avoid electron tunneling from the tip into the sample, because this results in charging the neutral O_2. Therefore, all AFM images in Fig. 1 were acquired at either zero or slightly negative sample bias (i.e., at a V_S located within the band gap of the n-type semiconducting TiO_2). The effect of tip-induced charging is shown in Fig. 2. Fig. 2*A* shows the anatase (101) surface after exposure to O_2 at $T = 5.5$ K. The same area was imaged in Fig. 2*B* but now a positive sample bias of +0.35 V was applied. The slow scanning direction is bottom-to-top and horizontal streaks in the image originate from tip-induced changes. Here the tip injects electrons into the neutral O_2 molecules and converts them to $(O_2)^-$. The resulting $(O_2)^-$ configuration is stable over the timescale of the experiment (many hours), even though the substrate is electrically conducting. A tunneling current image recorded simultaneously with Fig. 2*B* is shown in the inset. The tunneling current due to the charging of the neutral O_2 was below the detection limit of ≈0.1 pA.

The maximum concentration of the $(O_2)^-$ species that can be obtained by direct electron injection from the tip depends on the applied sample bias. This is shown in Fig. 2 *C* and *D*, where the same surface area is imaged after one scan at a bias of +0.44 and +1.1 V, respectively (an extended dataset is shown in Fig. S3). Fig. 2*D* shows that, after applying +1.1 V, almost all O_2 molecules are charged. A constant-height STM image ($V_S = +1.1$ V) of the same region is presented in Fig. 2*E*. It shows the molecular orbitals of the $(O_2)^-$ species as reported in a previous STM study (28), together with the signature of subsurface dopants (blue arrows). Based on our previous work, we attribute these dopant defects to Nb^+ donors located in the first subsurface layer (28), because this model fits best with the observed surface chemistry (28, 29) and electronic structure (30) of the surface. When comparing the position of the originally charged $(O_2)^-$ in Fig. 2*A* with the location of the dopants, it is obvious that the electron transfer into the O_2 molecule is not limited to the defect site but readily occurs in defect-free regions as well. In our previous work, where oxygen dosing was performed at $T = 100$ K, we found that all $(O_2)^-$ adsorbed directly above the dopant site (28). We conclude that the activated $(O_2)^-$ species diffuse toward the Nb^+ dopants at elevated temperatures due to an electrostatic interaction.

Temperature-Programmed Desorption and XPS. To assess thermal stability and charge state of the two O_2 species we resort to area-averaging spectroscopies. Fig. 3*A* shows temperature-programmed desorption (TPD) spectra with increasing O_2 exposure. The desorption peak at 64 K saturates at a coverage corresponding to a full monolayer, then a multilayer peak appears at 34 K. The monolayer peak shows first-order behavior with a desorption temperature corresponding to an adsorption energy

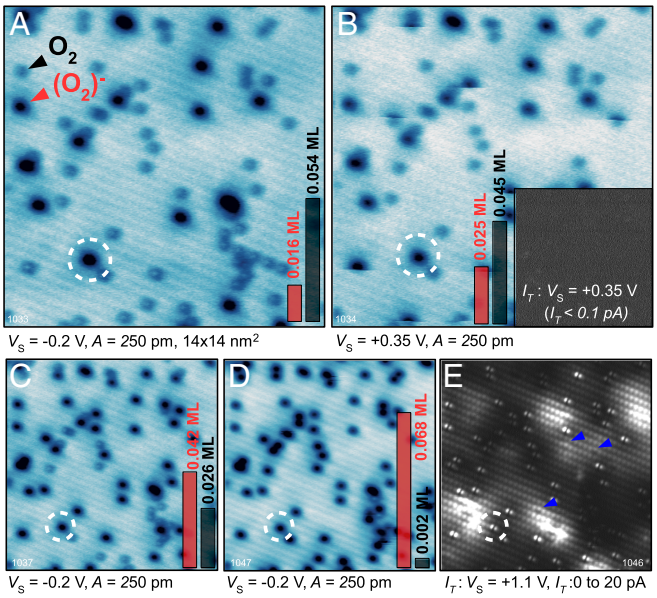

Fig. 2. Injecting electrons into O_2 by the STM tip. (*A*) AFM image of the anatase (101) surface after exposure to O_2. Note that no electron injection occurs at a negative sample bias of $V_S = -0.2$ V. (*B*) Scanning the same region at a positive sample bias of +0.35 V. (*Inset*) The simultaneously recorded tunneling current. (*C* and *D*) The same area following scans at V_S = +0.44 V and +1.1 V, respectively. (*E*) Constant-height STM image of the same region. Blue arrows mark subsurface Nb^+ dopants. Dashed circles mark the same position in all panels.

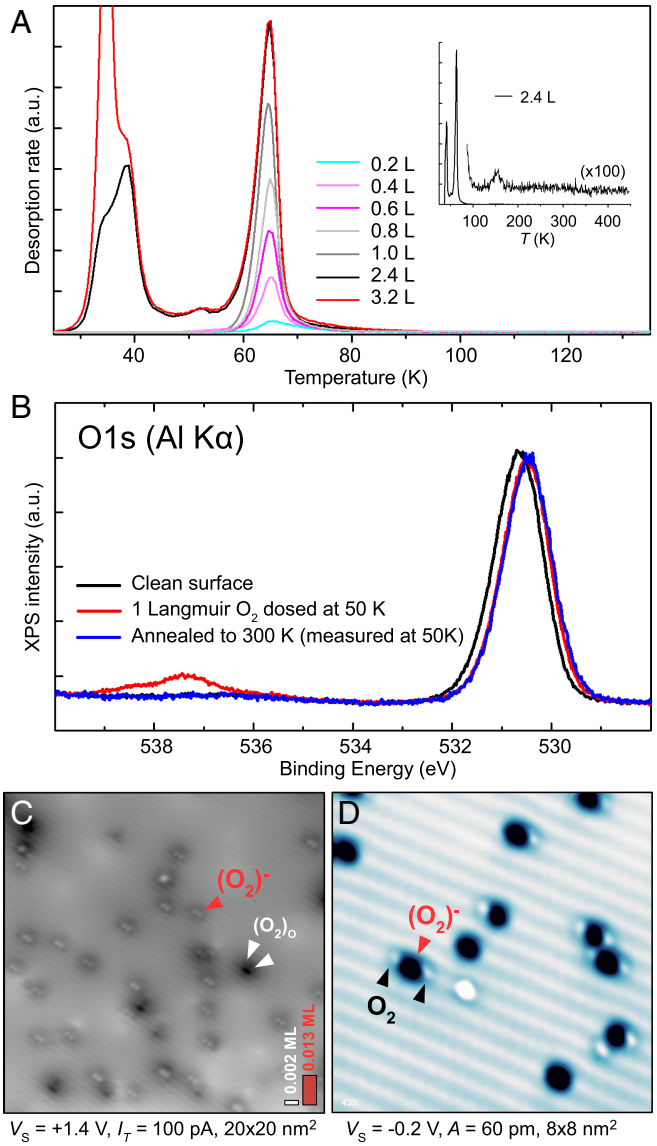

Fig. 3. Temperature-dependent behavior. (*A*) TPD spectra of O_2 from the anatase (101) surface. (*Inset*) A larger temperature range. (*B*) XPS spectra of the O1s peak for a clean anatase (101) surface and after exposure to 1 Langmuir (L) of oxygen. (*C*) STM image of the anatase (101) surface after dosing 1 ML O_2 at $T < 15$ K and subsequent annealing to room temperature. The red arrow marks an $(O_2)^-$ molecule; the pair of white arrows mark a dissociated O_2. (*D*) AFM image of the surface after dosing 0.04 ML O_2 and annealing to 35 K. Neutral O_2 diffused toward the $(O_2)^-$.

of 0.19 ± 0.02 eV (assuming a prefactor of 10^{15} s^{-1}). The only other desorption peak occurs at 150 K (Fig. 3*A*, *Inset*); it corresponds to just 0.003 ML O_2. This peak might be related to O_2 adsorbed at step sites (31).

Whereas TPD suggests no O_2 desorption above 150 K, STM imaging clearly shows that the $(O_2)^-$ species are stable even above room temperature. Fig. 3*C* shows an STM image of the anatase surface following exposure to 1 L O_2 at $T < 15$ K, and subsequent annealing to 300 K. An $(O_2)^-$ density of 0.013 ML is observed (red arrows), with the same STM appearance as the $(O_2)^-$ in Fig. 2*E*. A few molecules dissociate at room temperature (marked by white arrows) and split into pairs of bridging oxygen dimers [referred to as $(O_2)_O$ in previous work (28)]. It is interesting to note that the neutral O_2 molecules can diffuse across the surface at temperatures above ≈25 K and are attracted to the $(O_2)^-$ (Fig. 3*D*). Such clustering was also reported to occur in the gas phase (32).

XPS provides independent confirmation of the charge state of the adsorbed O_2 species (Fig. 3*B*). The black curve in Fig. 3*B* shows XPS of the O1s state on the clean surface, with a peak at $E_B = 530.7$ eV originating from lattice oxygen. Exposing the surface to 1 L O_2 at 50 K (red curve) results in a new feature at ≈537.3 eV; this double peak is due to final state effects and a characteristic of physisorbed oxygen in the triplet state (33). In addition, the peak of the lattice oxygen shifts toward lower binding energies due to an upward band bending of 0.19 eV. Annealing the surface to room temperature (blue curve) results in desorption of the triplet O_2 and the disappearance of the peak at 537.3 eV. The band bending remains, however, because it is induced by the ≈0.013 ML of chemisorbed $(O_2)^-$ (estimated from Fig. 3*C*). The entire monolayer of triplet O_2 therefore does not contribute to the band bending, which confirms their neutral charge state.

Kelvin Probe Spectroscopy and Charge Manipulation. For a quantitative evaluation of charging the neutral O_2, and the reverse process of removing an electron from the $(O_2)^-$, we used point Kelvin probe spectroscopy (34). We positioned the tip above a single, neutral O_2 molecule and ramped up the V_S, to switch its charge state to $(O_2)^-$. The corresponding Kelvin parabola is shown as the black curve in Fig. 4*A*. The step at $V_S \approx +0.35$ V corresponds to the charging event, and a simultaneous jump to a different parabola with its maximum shifted toward a higher V_S. Such a change in the local contact potential difference (LCPD) reflects upward band bending induced by negative charge localized at the molecule. The typical LCPD shift due to charging is 0.2 to 0.5 eV. The vertical jump in frequency shift (black curve in Fig. 4*A*) is induced by the chemical activation of the molecule; the attractive force is significantly higher after switching to the $(O_2)^-$ state.

When ramping the V_S down to negative values a discharging occurs typically at $V_S \approx -1.5$ V (red curve). During this process molecules often move away, as discussed in the context of Fig. 4 *C*–*F*. They desorb, hop by several adsorption positions, or jump to the tip apex. We attribute this mobility to the sudden transition between the chemisorbed and physisorbed states, that is, a Newns–Anderson process (35) as sketched in Fig. 4*B*. The physisorbed molecule has a shallow potential minimum far from the surface, whereas the chemisorbed state has a much deeper minimum nearer to the surface. Electron removal from the $(O_2)^-$ results in a neutral molecule too close to the surface, which is immediately and strongly repelled. We note that for all tip-induced charging and discharging events throughout this work we retracted the tip by $\Delta z = +50$ pm compared with normal imaging conditions. This reduces the probability of transferring the molecule to the tip apex. Further, we note that the $(O_2)^-$ molecule used in Fig. 4*A* hopped by two lattice constants during the discharging process; the gray parabola is therefore still affected by this molecule.

Fig. 4 *C*–*F* focus on discharging the $(O_2)^-$ and its consequent motion at the surface. The surface in Fig. 4*C* contains a mixture of O_2 and $(O_2)^-$. Bias sweeps down to −1.8 V were applied above three $(O_2)^-$ molecules (red arrows), and Fig. 4*D* shows the same region afterward. Molecules 1 and 2 have disappeared. During this process the substrate gains the excess electrons back, and this charge is accepted by other neutral molecules adsorbed nearby (white arrows). Molecule 3 moved by one adsorption site after the discharging, and one neighboring, neutral molecule has become charged. Finally, one new, neutral O_2 has appeared in the region (marked by a circle), which is likely molecule 1 or 2.

The negative bias sweeps were applied above all $(O_2)^-$ species in Fig. 4*D*, which resulted in further desorption and charge rearrangement in the area (see Fig. 4*E*). The same action was

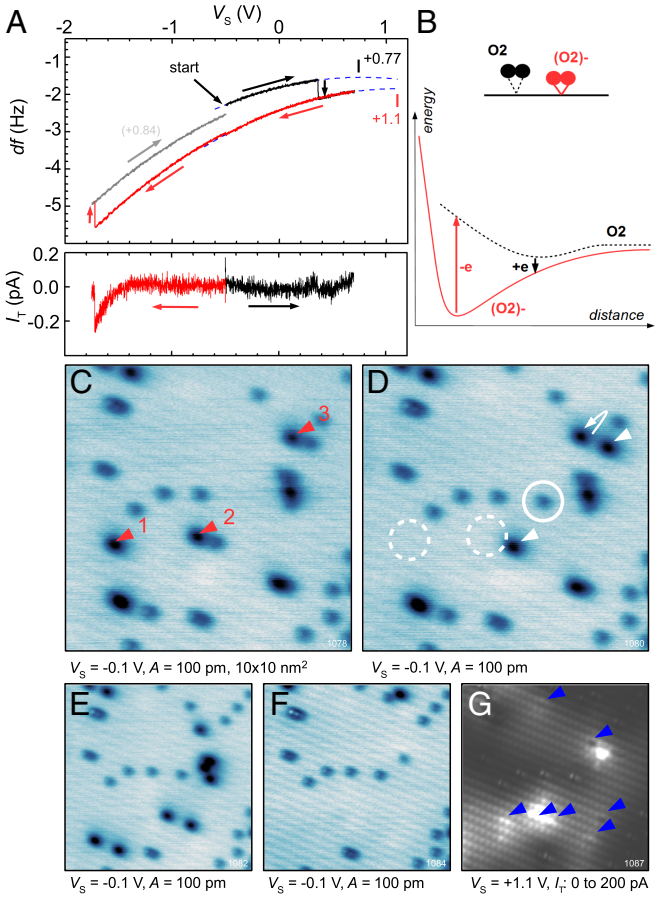

Fig. 4. Point spectroscopy. (*A*) Kelvin parabolas showing charging and discharging an O_2 molecule (*Upper*) and the simultaneously recorded tunneling current (*Lower*). (*B*) Schematic potential-energy curves for adsorbed O_2 and $(O_2)^-$. (*C*) Surface with adsorbed O_2; bias sweeps down to −1.8 V were applied above the marked molecules. (*D*) The same area afterward; see the text for a description of the changes. (*E* and *F*) The same area after applying further negative-bias sweeps above all $(O_2)^-$. (*G*) STM image of the same region as in *F*; blue arrows mark Nb^+ dopants.

repeated once again, and the result is shown in Fig. 4*F*. Here the neutral O_2 species do not spontaneously accept the electrons any further. We attribute it to the excess electrons being spatially confined around subsurface Nb^+ dopants (30). The dopants (blue arrows) within the region are clearly visible in STM (Fig. 4*G*); spontaneous charging events in Fig. 4 *C*–*F* occurred exclusively in their vicinity.

The tunneling current was recorded simultaneously with the Kelvin parabola measurements (Fig. 4a, *Lower*). The charging is typically accompanied with a negligible tunneling current. Before the discharging event, however, we reproducibly detect a small current of the order 1 pA, which abruptly stops. We attribute this to a tunneling from an occupied orbital of the $(O_2)^-$ molecule. The excess electron of the $(O_2)^-$ therefore has an energy in the middle of the band gap and facilitates chemical bonding with the substrate. This bond is broken when the electron is removed.

Charge-Transfer Limitation. The concentration of intrinsic $(O_2)^-$, in the absence of tip-induced charging, is only ≈0.01 ML. Charge transfer between the substrate and adsorbed molecules is a decisive factor in catalytic processes such as the oxygen reduction reaction (38, 39), so it is worthwhile investigating why so few molecules become charged. In Fig. 5 we propose a simple model. For a clean surface (Fig. 5*A*), the adsorbed, neutral O_2 molecule has its lowest unoccupied molecular orbital (LUMO) state slightly below the anatase Fermi level (E_F); spontaneous charging can occur. Formation of the first $(O_2)^-$ species induces upward band bending, which shifts the LUMO of subsequently adsorbed, neutral O_2 molecules above E_F and prevents the charging of additional molecules.

Despite this intrinsic limitation electrons can still be injected using the tip, but it is necessary to overcome the energy barrier due to built-up band bending by applying an increasingly positive sample bias V_S. To test this model, we have investigated the tip-induced charging in detail. We selected an area with a relatively high concentration of adsorbed neutral O_2 (such as in Fig. 2*A*). As the molecules were charged one by one we measured Kelvin parabolas above each of them, as in Fig. 4*A*. Fitting the parabola provides the LCPD, which is directly proportional to the band bending. For each parabola we can also determine the value of V_S where the charging event occurs. There is clearly a linear correlation between these two quantities as plotted in Fig. 5*C*. In other words, the LCPD shifts to positive values with increasing $(O_2)^-$ concentration (an indication of upward band bending). The bias necessary for charging the neutral molecules shifts in proportion. The experiment was repeated with three different tips (different colors in Fig. 5*C*); in all cases a linear correlation with a slope close to unity was observed. The offsets

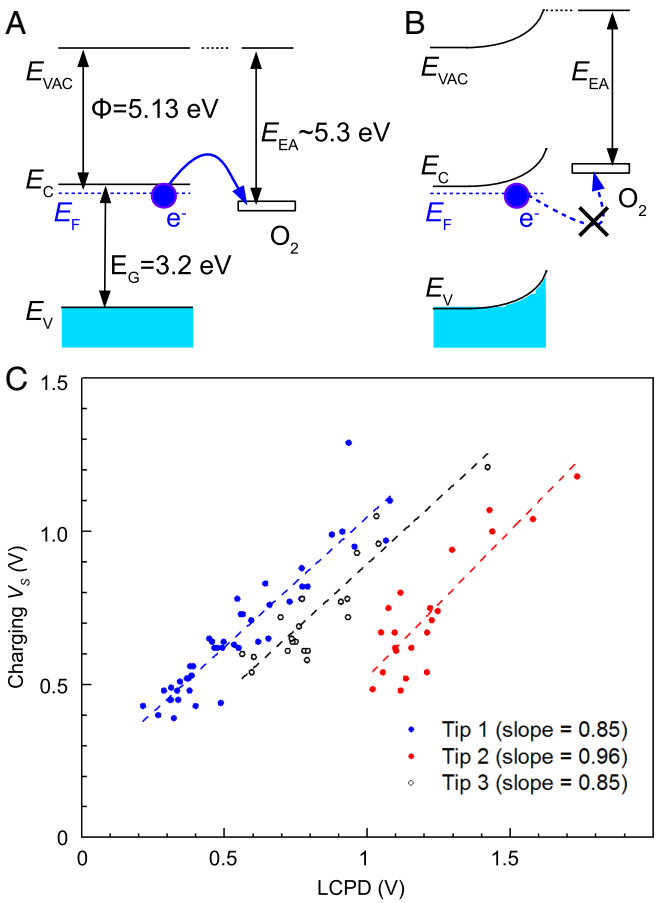

Fig. 5. Limitation to charge transfer. (*A* and *B*) Model of the electron transfer based on band bending. In *A* the O_2 affinity level for accepting an electron lies below the Fermi level of anatase, and thus electron transfer is possible. In *B* adsorbed $(O_2)^-$ induce upward band bending; the empty O_2 level shifts above the anatase Fermi level and electron transfer to further neutral O_2 molecules is blocked. Experimental values of the work function Φ and the band gap E_g are adopted from refs. 36 and 37. (*C*) Measured relation between the LCPD and V_S required for charging a molecule. For details see the text.

of the LCPD result from different tip work functions. The LCPD plotted on the x axis corresponds to the value before the charging event (i.e., the black parabola in Fig. 4*A*). A more detailed description of the experiment is given in the Fig. S4.

From the band bending observed upon O_2 adsorption (XPS data in Fig. 3) we deduce that the LUMO state of the neutral O_2 is initially not more than 0.19 eV below the anatase E_F. Assuming an anatase work function of 5.1 eV (36), this corresponds to an electron affinity of 5.1 to 5.3 eV (Fig. 5*A*). Considering that the triplet O_2 is only physisorbed, its electron affinity is strikingly different from an O_2 molecule in the gas phase, where the affinity is 0.45 eV (40). Upon approaching toward solid surfaces, molecular electron affinities are increased due to effects such the image charge (41), Madelung potential (42), surface electric dipoles, and quantum-mechanical interaction with the surface. Our results indicate that the electron affinity of the physisorbed molecule, and thus the exact physisorbed configuration, play a key role in the charge transfer.

UV Light. In this section we show that exposing the sample to UV irradiation induces dis/charging events identical to those achieved by STM/AFM manipulation. We started with an anatase (101) surface containing a mixture of O_2 and $(O_2)^-$ (Fig. 6*A*) and irradiated the sample for 10 min ($T < 12$ K). Fig. 6*B* shows the same area after the UV exposure, and Fig. 6*C* after an additional 80 min of UV light. The overall coverage decreases; the red and black bars in Fig. 6 *A*–*C* give the amount of charged and uncharged O_2 molecules, respectively. In addition, some dissociation occurred (discussed below).

A sketch of possible events is outlined in Fig. 6*D*. UV illumination introduces holes in the valence band and excess electrons in the conduction band. It is known (13, 20) that holes induce the desorption of $(O_2)^-$. This process is akin to removing the electron by the STM tip at negative biases. Neutral O_2 molecules can accept electrons, either the ones photoexcited by the UV light or provided by dopants. The latter process becomes possible once the other $(O_2)^-$ species are photodesorbed. Some dissociated O_2 are highlighted by white arrows in Fig. 6*C*. These appear as a pair of adjacent, negatively charged species in AFM images. Using STM (dashed region and inset in Fig. 6*C*) we can clearly identify them based on our previous work (28, 43). Earlier (28) we found that the $(O_2)^-$ species dissociate upon scanning at $V_S > +2$ V; we thus attribute the photodissociation in Fig. 6*C* to hot electrons excited higher into the conduction band.

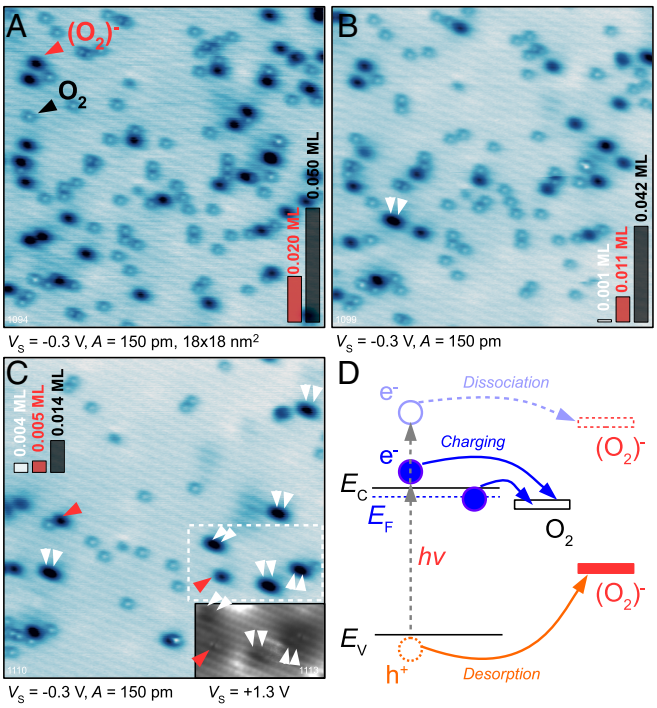

Fig. 6. Illuminating the sample by UV light. (*A*) Anatase (101) surface with adsorbed O_2. (*B*) The same region after exposing to UV light for 10 min. (*C*) The same region after another 80 min of UV illumination. (*D*) Schematic drawings of the processes occurring during the UV illumination.

Discussion

We have observed that exposing the anatase (101) surface to molecular oxygen results in the activation of 0.01–0.02 ML O_2 and a concomitant upward band bending of 0.19 eV in the substrate. The amount of charged (i.e., activated) oxygen could be increased approximately by a factor of five via tip-induced electron injection, resulting in a band bending up to 0.9 eV (Fig. 5*C*). The adsorption of O_2 has been studied in detail on the prototypical rutile (110) surface (11), and it is well accepted that an electron transfer is a prerequisite for O_2 chemisorption. This was first proved by integral techniques, mainly a combination of TPD, photodesorption, and electron-stimulated desorption (12, 14–19). The excess electrons on the rutile (110) surface are mainly provided by surface oxygen vacancies (22, 23, 44), although subsurface Ti interstitials also play a role (21). The anatase (101) surface typically does not contain any oxygen vacancies (45, 46), and the electrons are provided solely by subsurface dopants. The substrate n-type doping level then determines the concentration of adsorbed $(O_2)^-$ species through band bending (47).

Although the integral methods clearly prove the presence of molecular O_2 at the rutile (110) surface, STM studies have mainly focused on dissociated oxygen, that is, O adatoms (22, 23). The key problem in using STM for O_2 adsorption is its sensitivity to injected electrons. We have shown that STM imaging converts neutral O_2 molecules into $(O_2)^-$. The $(O_2)^-$ species may be further dissociated by the tip; the exact conditions vary with the substrate (24, 28, 48). AFM can image all of the species with atomic resolution without the need of tunneling current, which makes this method an invaluable tool for studying systems sensitive to electron injection.

AFM experiments with molecule charging have previously been performed on insulating materials, typically NaCl thin films (8, 49, 50), which decouple the adsorbate from a metal substrate. Even though the anatase sample is electrically conducting, two stable charge states of O_2 could be observed. This is due to the large hysteresis between the charging and discharging events (Fig. 4*A*), a special property of the O_2 molecule. The charging/discharging is accompanied with a large structural relaxation, that is, a transition between the physisorbed and chemisorbed state (6, 25).

The tip-induced discharging is accompanied by a measurable tunneling current (Fig. 4*A*), which we explain in the following way. After removing the excess electron from the $(O_2)^-$, the molecule must relax away from the surface. The excess electron can be replenished from the conducting substrate during this period. The quantum efficiency of the tip-induced discharging is of the order 10^{-6}; this estimate comes from integrating the tunneling current under the red curve in Fig. 4*A*. The UV illumination in Fig. 6 has a comparable quantum efficiency, as estimated from the incident photon flux, illumination time, and number of photodesorption events. Comparable quantum efficiencies support the picture that the tip-induced and light-induced events have the same origin.

Conclusions

We have shown that AFM can resolve different chemical states of a single O_2 molecule, as well as switch the chemical state by

injecting or removing an electron. The tip-induced charging transitions are identical to those occurring when the surface is illuminated by UV light, or when electrons are spontaneously transferred from subsurface dopants. The methodology presented here opens a pathway for investigating and understanding key processes in photocatalysis, electrochemistry, or redox chemistry. Our results indicate that the physisorbed molecular state, in particular its electron affinity, plays a key role in the electron transfer. The concentration of activated $(O_2)^-$ species is limited by a counteracting mechanism, which originates from band bending induced by electric charge localized at these species. The dopant (defect) sites have little direct influence on the charge transfer and only enter the process indirectly by providing the excess charge.

Materials and Methods

Combined STM/AFM measurements were performed at $T = 4.8$ K in an ultrahigh vacuum (UHV) chamber with a base pressure below 2×10^9 Pa, equipped with a commercial Omicron q-Plus LT head. O_2 was dosed directly into the cryostat at $T = 5.5$ K. Tuning-fork-based AFM sensors with a separate wire for the tunneling current were used (51) ($k = 3{,}750$ N/m, $f_0 = 47{,}500$ Hz, $Q \approx 50{,}000$). Electrochemically etched W tips were glued to the tuning fork and cleaned in situ by field emission and self-sputtering in 10^{-4} Pa Ar (52). The reactive tip termination was reproducibly obtained by touching the anatase surface and applying a high tunneling current (53). The short-range chemical forces in Fig. 1*D* were determined by measuring $\Delta f(z)$ curves above the O_2 molecules, subtracting the long-range contribution (54) and converting the frequency shift to force (55). We used a single-crystalline mineral anatase TiO_2 (101) sample, naturally doped by 1% Nb. The surface was prepared by ex situ cleaving and subsequent cleaning in vacuum by cycles of Ar^+ sputtering (1 keV) and annealing to 950 K (56).

The TPD and XPS measurements were carried out in a UHV system with a base pressure of 5×10^{-9} Pa. The anatase sample was mounted on a Ta back plate, cooled by a Janis ST-400 UHV liquid-He flow cryostat, and heated by direct current through the back plate. The temperature was measured by a K-type thermocouple spot-welded to the sample plate; the temperatures are accurate within ± 3 K. O_2 was dosed by an effusive molecular beam with a hat-shape profile (57). A linear temperature ramp of 1 K/s was used. A HIDEN quadrupole mass spectrometer in a line-of-sight configuration was used for detection of the TPD flux. The amount of dosed gases was calibrated according to the method described in ref. 58. One monolayer is defined as 1 molecule per surface 5-coordinated titanium atom and corresponds to an exposure of 1.6 Langmuir (L; 1 L = 1.33×10^{-4} Pa$\times$s). The calibration includes a sticking coefficient of $\approx$0.9. Analysis of TPD spectra was done according to the procedure in ref. 59. XPS spectra were measured with a hemispherical electrostatic energy analyzer (SPECS Phoibos 150), using a monochromatized Al Kα X-ray source (SPECS Focus 500) at a sample temperature of $T = 50$ K. XPS was measured under a 60° exit angle off normal. An Hg discharge lamp was used for illuminating the sample by UV light. The incident photon flux was 1.3×10^{16} $cm^{-2}s^{-1}$. UV illumination was introduced to the UHV chamber via a quartz window. The sample temperature during the illumination was below 12 K.

ACKNOWLEDGMENTS. The work was supported by the European Research Council (ERC) advanced grant "Oxide Surfaces" (ERC-2011-ADG-20110209), by the Austrian Science Fund (FWF) project Wittgenstein Prize (Z 250), and FWF START Grant Y847-N20.

1. Hayyan M, Hashim MA, AlNashef IM (2016) Superoxide ion: Generation and chemical implications. *Chem Rev* 116:3029–3085.
2. Schweitzer C, Schmidt R (2003) Physical mechanisms of generation and deactivation of singlet oxygen. *Chem Rev* 103:1685–1757.
3. Bugg TH (2003) Dioxygenase enzymes: Catalytic mechanisms and chemical models. *Tetrahedron* 59:7075–7101.
4. Costas M, Mehn MP, Jensen MP, Que L (2004) Dioxygen activation at mononuclear nonheme iron active sites: Enzymes, models, and intermediates. *Chem Rev* 104: 939–986.
5. Freund HJ, Roberts MW (1996) Surface chemistry of carbon dioxide. *Surf Sci Rep* 25:225–273.
6. Libisch F, Huang C, Liao P, Pavone M, Carter EA (2012) Origin of the energy barrier to chemical reactions of O_2 on Al(111): Evidence for charge transfer, not spin selection. *Phys Rev Lett* 109:198303.
7. Hofmann OT, Rinke P, Scheffler M, Heimel G (2015) Integer versus fractional charge transfer at metal(/insulator)/organic interfaces: Cu(/NaCl)/TCNE. *ACS Nano* 9:5391–5404.
8. Gross L, Mohn F, Liljeroth P, Giessibl FJ, Meyer G (2009) Measuring the charge state of an adatom with noncontact atomic force microscopy. *Science* 324:1428–1431.
9. Steurer W, Fatayer S, Gross L, Meyer G (2015) Probe-based measurement of lateral single-electron transfer between individual molecules. *Nat Commun* 6:8353.
10. Linsebigler AL, Lu G, Yates JT (1995) Photocatalysis on TiO_2 surfaces: Principles, mechanisms, and selected results. *Chem Rev* 95:735–758.
11. Dohnalek Z, Lyubinetsky I, Rousseau R (2010) Thermally-driven processes on rutile TiO_2 (110)-(1 $\times$ 1): A direct view at the atomic scale. *Prog Surf Sci* 85:161–205.
12. Henderson MA, Epling WS, Perkins CL, Peden CHF, Diebold U (1999) Interaction of molecular oxygen with the vacuum-annealed TiO_2(110) surface: Molecular and dissociative channels. *J Phys Chem B* 103:5328–5338.
13. Thompson TL, Yates JT (2005) Monitoring hole trapping in photoexcited TiO_2(110) using a surface photoreaction. *J Phys Chem B* 109:18230–18236.
14. Kimmel GA, Petrik N (2008) Tetraoxygen on reduced TiO_2(110): Oxygen adsorption and reactions with bridging oxygen vacancies. *Phys Rev Lett* 100:196102.
15. Petrik NG, Kimmel GA (2010) Photoinduced dissociation of O_2 on rutile TiO_2(110). *J Phys Chem Lett* 1:1758–1762.
16. Petrik NG, Kimmel G (2011) Electron- and hole-mediated reactions in UV-irradiated O_2 adsorbed on reduced rutile TiO_2(110). *J Phys Chem C* 115:152–164.
17. Zhang Z, Yates JT (2010) Effect of adsorbed donor and acceptor molecules on electron stimulated desorption: O_2/TiO_2(110). *J Phys Chem Lett* 1:2185–2188.
18. Henderson MA, Shen M, Wang ZT, Lyubinetsky I (2013) Characterization of the active surface species responsible for UV-induced desorption of O_2 from the rutile TiO_2(110) surface. *J Phys Chem C* 117:5774–5784.
19. Wang ZT, Deskins NA, Lyubinetsky I (2012) Direct imaging of site-specific photocatalytical reactions of O_2 on TiO_2(110). *J Phys Chem Lett* 3:102–106.
20. Thompson TL, Yates JT (2006) Surface science studies of the photoactivation of TiO_2 – New photochemical processes. *Chem Rev* 106:4428–4453.
21. Wendt S, et al. (2008) The role of interstitial sites in the Ti3d defect state in the band gap of titania. *Science* 320:1755–1759.
22. Lira E, et al. (2010) Dissociative and molecular oxygen chemisorption channels on reduced rutile TiO_2(110): An STM and TPD study. *Surf Sci* 604:1945–1960.
23. Lira E, et al. (2012) Effects of the crystal reduction state on the interaction of oxygen with rutile TiO_2 (110). *Catal Today* 182:25–38.
24. Tan S, et al. (2011) Molecular oxygen adsorption behaviors on the rutile TiO_2(110)-1$\times$1 surface: An in situ study with low-temperature scanning tunneling microscopy. *J Am Chem Soc* 133:2002–2009.
25. Li YF, Aschauer U, Chen J, Selloni A (2014) Adsorption and reactions of O_2 on anatase TiO_2. *Acc Chem Res* 47:3361–3368.
26. Li YF, Selloni A (2013) Theoretical study of interfacial electron transfer from reduced anatase TiO_2 (101) to adsorbed O_2. *J Am Chem Soc* 135:9195–9199.
27. Yurtsever A, et al. (2012) Understanding image contrast formation in TiO_2 with force spectroscopy. *Phys Rev B* 85:125416.
28. Setvin M, et al. (2013) Reaction of O_2 with subsurface oxygen vacancies on TiO_2 anatase (101). *Science* 341:988–991.
29. Setvin M, et al. (2015) A multitechnique study of CO adsorption on the TiO_2 anatase (101) surface. *J Phys Chem C* 119:21044–21052.
30. Setvin M, et al. (2014) Direct view at excess electrons in TiO_2 rutile and anatase. *Phys Rev Lett* 113:086402.
31. Setvin M, et al. (2014) Charge trapping at the step edges of TiO_2 anatase (101). *Angew Chem Int Ed Engl* 53:4714–4716.
32. DeLuca MJ, Han CC, Johnson MA (1990) Photoabsorption of negative cluster ions near the electron detachment threshold: A study of the $(O_{2n})^-$ system. *J Chem Phys* 93:268.
33. Puglia C, et al. (1995) Physisorbed, chemisorbed and dissociated O_2 on Pt(111) studied by different core level spectroscopy methods. *Surf Sci* 342:119–133.
34. Sadewasser S, Glatzel T (2012) *Kelvin Probe Force Microscopy* (Springer, Berlin).
35. Newns DM (1969) Self-consistent model of hydrogen chemisorption. *Phys Rev* 178:1123–1135.
36. Xiong G, et al. (2007) Photoemission electron microscopy of TiO_2 anatase films embedded with rutile nanocrystals. *Adv Func Mater* 17:2133–2138.
37. Scanlon DO, et al. (2013) Band alignment of rutile and anatase TiO_2. *Nat Mater* 12:798–801.
38. Wang B (2005) Recent development of non-platinum catalysts for oxygen reduction reaction. *J Power Sources* 152:1–15.
39. Setvin M, et al. (2016) Following the reduction of oxygen on TiO_2 anatase (101) step by step. *J Am Chem Soc* 138:9565–9571.
40. Sulka M, Pitonak M, Neogrady P, Urban M (2008) Electron affinity of the O_2 molecule: CCSD(T) calculations using the optimized virtual orbitals space approach. *Int J Quant Chem* 108:2159–2171.
41. Lundqvist BI, et al. (1983) Theoretical studies of molecular adsorption on metal surfaces. *Int J Quant Chem* 23:1083–1090.
42. Borisov AG, Sidis V (1997) Theory of negative-ion conversion of neutral atoms in grazing scattering from alkali halide surfaces. *Phys Rev B* 56:10628–10643.
43. Setvin M, et al. (2014) Identification of adsorbed molecules via STM tip manipulation: CO, H_2O, and O_2 on TiO_2 anatase(101). *Phys Chem Chem Phys* 16:21524–21530.
44. Diebold U (2003) The surface science of titanium dioxide. *Surf Sci Rep* 48:53–299.
45. He Y, Dulub O, Cheng HZ, Selloni A, Diebold U (2009) Evidence of the predominance of the subsurface defects on reduced anatase TiO_2(101). *Phys Rev Lett* 102:106105.
46. Scheiber P, et al. (2012) (Sub)Surface mobility of oxygen vacancies at the TiO_2 anatase(101) surface. *Phys Rev Lett* 109:136103.

47. Zhang Z, Yates JT (2012) Band bending in semiconductors: Chemical and physical consequences at surfaces and interfaces. *Chem Rev* 112:5520–5551.
48. Cui Y, et al. (2013) Adsorption, activation, and dissociation of oxygen on doped oxides. *Angew Chem Int Ed Engl* 52:11385–11387.
49. Steurer W, et al. (2015) Manipulation of the charge state of single Au atoms on insulating multilayer films. *Phys Rev Lett* 114:036801.
50. Repp J, et al. (2016) Charge-state-dependent diffusion of individual gold adatoms on ionic thin NaCl films. *Phys Rev Lett* 117:146102.
51. Giessibl FJ (2012) Sensor for noncontact profiling of a surface. US Patent 2012/0131704 A1.
52. Setvin M, et al. (2012) Ultrasharp tungsten tips—Characterization and nondestructive cleaning. *Ultramicroscopy* 113:152–157.
53. Stetsovych O, et al. (2015) Atomic species identification at the (101) anatase surface by simultaneous scanning tunnelling and atomic force microscopy. *Nat Commun* 6:7265.
54. Lantz MA, et al. (2001) Quantitative measurement of short-range chemical bonding forces. *Science* 291:2580–2583.
55. Sader JE, Jarvis SP (2004) Accurate formulas for interaction force and energy in frequency modulation force spectroscopy. *Appl Phys Lett* 84:1801–1803.
56. Setvin M, et al. (2014) Surface preparation of TiO_2 anatase (101): Pitfalls and how to avoid them. *Surf Sci* 626:61–67.
57. Halwidl D (2016) Development of an effusive molecular beam apparatus. (Springer, Berlin).
58. Pavelec J, et al. (2017) A multi-technique study of CO_2 adsorption on Fe_3O_4 magnetite. *J Phys Chem C* 146:014701.
59. Tait SL, Dohnalek Z, Campbell CT, Kay BD (2005) n-alkanes on MgO(100). I. Coverage-dependent desorption kinetics of n-butane. *J Chem Phys* 122:164707.
60. Sanchez-Sanchez C, et al. (2010) Understanding atomic-resolved STM images on TiO_2(110)-(1$\times$1) surface by DFT calculations. *Nanotechnology* 21:405702.
61. Enevoldsen GH, Glatzel T, Christensen MC, Lauritsen JV, Besenbacher F (2008) Atomic scale kelvin probe force microscopy studies of the surface potential variations on the TiO_2(110) surface. *Phys Rev Lett* 100:236104.